Virologica Sinica 38 (2023) 741–754

Contents lists available at ScienceDirect

Virologica Sinica

journal homepage: www.keaipublishing.com/en/journals/virologica-sinica
www.virosin.org

Research Article

RIPK3 promotes hantaviral replication by restricting JAK-STAT signaling without triggering necroptosis

Yue Si [a,1], Haijun Zhang [b,c,1], Ziqing Zhou [a,1], Xudong Zhu [a], Yongheng Yang [a], He Liu [a], Liang Zhang [a], Linfeng Cheng [a], Kerong Wang [a], Wei Ye [a], Xin Lv [a], Xijing Zhang [d], Wugang Hou [d], Gang Zhao [b,e], Yingfeng Lei [a,*], Fanglin Zhang [a,*], Hongwei Ma [a,d,*]

[a] Department of Microbiology, School of Basic Medicine, Air Force Medical University, Xi'an, 710032, China
[b] Department of Neurology, Xijing Hospital, Air Force Medical University, Xi'an, 710032, China
[c] Center of Clinical Aerospace Medicine, School of Aerospace Medicine, Key Laboratory of Aerospace Medicine of Ministry of Education, Air Force Medical University, Xi'an, 710032, China
[d] Department of Anesthesiology & Critical Care Medicine, Xijing Hospital, Air Force Medical University, Xi'an, 710032, China
[e] The College of Life Sciences and Medicine, Northwest University, Xi'an, 710069, China

ARTICLE INFO

Keywords:
Hantaan virus (HTNV)
RIPK3
Interferons
IFN-stimulated genes
STAT1
Innate immune response

ABSTRACT

Hantaan virus (HTNV) is a rodent-borne virus that causes hemorrhagic fever with renal syndrome (HFRS), resulting in a high mortality rate of 15%. Interferons (IFNs) play a critical role in the anti-hantaviral immune response, and IFN pretreatment efficiently restricts HTNV infection by triggering the expression of a series of IFN-stimulated genes (ISGs) through the Janus kinase-signal transducer and activator of transcription 1 (JAK-STAT) pathway. However, the tremendous amount of IFNs produced during late infection could not restrain HTNV replication, and the mechanism remains unclear. Here, we demonstrated that receptor-interacting protein kinase 3 (RIPK3), a crucial molecule that mediates necroptosis, was activated by HTNV and contributed to hantavirus evasion of IFN responses by inhibiting STAT1 phosphorylation. RNA-seq analysis revealed the upregulation of multiple cell death-related genes after HTNV infection, with RIPK3 identified as a key modulator of viral replication. RIPK3 ablation significantly enhanced ISGs expression and restrained HTNV replication, without affecting the expression of pattern recognition receptors (PRRs) or the production of type I IFNs. Conversely, exogenously expressed RIPK3 compromised the host's antiviral response and facilitated HTNV replication. RIPK3$^{-/-}$ mice also maintained a robust ability to clear HTNV with enhanced innate immune responses. Mechanistically, we found that RIPK3 could bind STAT1 and inhibit STAT1 phosphorylation dependent on the protein kinase domain (PKD) of RIPK3 but not its kinase activity. Overall, these observations demonstrated a noncanonical function of RIPK3 during viral infection and have elucidated a novel host innate immunity evasion strategy utilized by HTNV.

1. Introduction

Hantaan virus (HTNV), the prototype hantavirus (belonging to the *Bunyavirales* order and *Hantaviridae* family) carried by *Apodemus agrarius*, is a widespread zoonotic virus with negative-sense RNA genomes. The segmented genome of HTNV is composed of small (*S*), medium (*M*) and large (*L*) parts, which encode the nucleocapsid protein (NP), glycoprotein precursor (GPC, further cleaved into the N-terminal Gn and C-terminal Gc), and RNA-dependent polymerase protein (RdRp), respectively (Ning et al., 2021). HTNV is mainly transmitted to humans by infective aerosols from rodent excrements (Park et al., 2021), which causes severe hemorrhagic fever with renal syndrome (HFRS). Nearly 200,000 cases of HFRS are reported globally each year, most of which occur in Eurasia, especially in China (Lu et al., 2021). HFRS, a re-emerging infectious disease, is characterized by systemic inflammatory response syndrome and has a mortality rate of 5%–15% but unclear pathogenesis (Jiang et al., 2016; Kariwa et al., 2007; Tariq and Kim, 2022). Currently, no specific therapeutic strategies against hantaviruses are available. Host innate immune responses are the first line of defense against hantaviral infection and play an important role in eliminating viruses by bridging

* Corresponding authors.
E-mail addresses: yflei@fmmu.edu.cn (Y. Lei), flzhang@fmmu.edu.cn (F. Zhang), mahongwei0720@sina.com (H. Ma).
[1] Yue Si, Haijun Zhang and Ziqing Zhou contributed equally to this work.

https://doi.org/10.1016/j.virs.2023.08.006
Received 22 February 2023; Accepted 21 August 2023
Available online 25 August 2023

cellular and humoral immunity. Notably, hantaviruses have evolved multiple strategies to avoid host natural immune surveillance and clearance (Zhang et al., 2021). Elucidating their immune evasion mechanisms might be conducive to developing novel anti-hantaviral drugs.

Type I interferons (IFNs) and IFN-stimulated genes (ISGs) are crucial components of the host innate immune system. Pathogen-associated molecular patterns (PAMPs), including viral RNAs and proteins, can be sensed by host pattern recognition receptors (PRRs), thus eliciting robust antiviral IFN responses. PRRs recruit certain mediators (such as TRIF and MAVS) and protein kinases (e.g., TBK1), which further activate key transcription factors (e.g., IRF3 and IRF7) for IFN production (Lee and Ashkar, 2018; Schneider et al., 2014; Villarino et al., 2017). Secreted IFNs promote the transcription of various ISGs through the Janus kinase-signal transducer and activator of transcription (JAK/STAT) pathway to defend against viral infection (Zhang et al., 2021). Type I IFNs, including IFN-α and IFN-β, bind IFNAR1 and activate JAK, and JAK then phosphorylates STAT1 and STAT2. The STAT1-STAT2 heterodimer combines with IFN regulatory factor 9 (IRF9) to form the ISG factor 3 (ISGF3) complex, which can bind IFN-stimulated response elements (ISREs) and induce the transcription of ISGs (Mesev et al., 2019). Many ISGs, such as myxovirus resistance protein 1 (MX1), 2′-5′-oligoadenylate synthetase 1 (OAS1), and IFN-induced tetratricopeptide repeat protein 2 (IFIT2), perform antiviral functions by affecting the viral life cycle at different stages(Ye et al., 2015). IFN responses are crucial for hosts to restrict HTNV infection. Intriguingly, viruses have evolved the potent ability to evade host innate immune response (Wang et al., 2019). Previous studies also found that both the production of serum IFNs or other proinflammatory cytokines and the serum virus titer were positively correlated with HFRS disease severity (Wang et al., 2012), indicating that a hyperinflammatory environment with high levels of IFNs might not promote HTNV clearance but rather lead to HFRS pathogenesis. The mechanisms by which HTNV escapes from IFN-mediated immune responses remain to be determined.

Receptor-interacting protein kinase 3 (RIPK3) is a classic serine/threonine receptor-interacting protein kinase involved in necroptosis (Meng et al., 2021). During this process, RIPK1 activates RIPK3 by binding its RIP homotypic interaction motif (RHIM) upon stimulation with TNF-α or other death signals, and RIPK3 then recruits and phosphorylates mixed lineage kinase domain-like (MLKL) protein. MLKL oligomers are the executors of necroptosis, which can disrupt the membrane integrity and cause rupture of the cell membrane, eventually causing cell death and the leakage of abundant inflammatory factors. In addition to the widely accepted pro-necroptotic functions of RIPK3, RIPK3 is involved in modulating the IFN signaling pathways post-infection (Downey et al., 2017). For instance, lipopolysaccharide (LPS) stimulated RIPK3, acting through TLR4, could directly facilitate IFN-β production via the canonical TRIF-IRF3 pathway without triggering MLKL-mediated necroptosis in bone marrow-derived macrophages (BMDMs) (Saleh et al., 2017). Additionally, our previous research suggested that RIPK3 could inhibit the expression of antiviral IFN-induced protein 44-like gene (IFI44L), making neurons susceptible to Japanese encephalitis virus (JEV) infection (Bian et al., 2020). This dual role of RIPK3 against infection, as indicated by these seemingly contradictory results, might be related to the use of different pathogen strains or different stages of infection. It is unclear how RIPK3 regulates host anti-hantaviral immunity.

In this study, we found that RIPK3 was activated by HTNV without triggering cell death. RIPK3 promoted HTNV replication by inhibiting STAT1 phosphorylation and restricting ISGs expression. Moreover, RIPK3$^{-/-}$ mice challenged with HTNV showed prompt virus clearance and enhanced inflammatory responses that were characterized by prominent macrophage activation. Mechanistically, the protein kinase domain (PKD) of RIPK3 mediated its interaction with STAT1 and blocked STAT1 activation independent of the kinase activity of RIPK3. These findings demonstrated a previously unidentified role for RIPK3 in HTNV infection and revealed a novel immune evasion strategy utilized by HTNV.

2. Materials and methods

2.1. Plasmids and small interfering RNA (siRNA) transfection

All of the plasmids used in this experiment are listed in Supplementary Table S1. The plasmids were transfected into cells by using Hieff trans™ liposomal transfection reagent (Yeasen, China). Sequences used for RNA inhibition were synthesized by GenePharma (Shanghai, China). The siRNA sequences targeting Z-DNA-binding protein 1 (ZBP1), RIPK3 and MLKL are listed in Supplementary Table S2. Entranster™-R4000 (Engreen, China) was used for siRNA transfection.

2.2. Cell culture

HEK293T (CRL-3216), Huh-7 (SNL-085), A549 (CCL-185), and Vero E6 (TIB-152) cells were purchased from the American Type Culture Collection (ATCC) and cultured in Dulbecco's modified Eagle's medium (DMEM, Gibco, USA) with 10% fetal bovine serum (HyClone, Logan, UT) and a 1% penicillin–streptomycin–gentamicin solution (100×) in a humidified incubator with 95% air and 5% CO_2 at 37 °C. The murine fibroblast cell line L929 (CCL-1) was purchased from ATCC and cultured in RPMI medium 1640 with 10% or 20% FBS and a 1% penicillin–streptomycin–gentamicin solution (100×) at 37 °C. BMDMs were obtained from the bone marrow of C57BL/6J mice or RIPK3$^{-/-}$ mice and then immersed in sterile Dulbecco's phosphate-buffered saline (DPBS). After isolation of whole bone marrow cells from the tibia and femur, we cultured them in complete RPMI medium (Gibco, USA) for 7 days (1640 with 20% FBS: L929 supernatant = 1:3 in volume) (Heap et al., 2021).

2.3. Viral infection

HTNV strain 76-118 that had been stored in our laboratory was first expanded in Kunming suckling mice and subsequently propagated in Vero E6 cells. HTNV titers were determined by ELISA as previously described (Xu et al., 2002). JEV strain P3 was first expanded in suckling mice 3 days after birth. Brain tissue was harvested 3–5 days after injection when the mice had symptoms such as breast rejection and convulsion. One milliliter of serum-free DMEM was added to every 100 mg of brain tissue for grinding. The cell fragments were removed by centrifugation, filtered to obtain the virus suspension and titrated using a conventional plaque assay. Before viral infection, cells were rinsed with DPBS to remove excess serum and then cultured with the virus suspension at the desired MOI. After incubation for 90–120 min, the medium was replaced with complete medium.

2.4. Mouse experiments and sample preparation

Six-to eight-week-old female C57BL/6J mice (17–21 g) were purchased from the Experimental Animal Center of Air Force Medical University. RIPK3$^{-/-}$ C57BL/6J mice were kindly provided by Dr. Yazhou Wang (Department of Neurobiology and Collaborative Innovation Center for Brain Science, School of Basic Medicine, Air Force Medical University) (Bian et al., 2020).

DNA samples from newborn mice were amplified through PCR, and the resultant products were analyzed using agarose gel electrophoresis to screen for RIPK3$^{-/-}$ mice. The RIPK3 primer sequences were as follows:

Forward, 5′-AGAAGATGCAGCAGCCTCAGCT-3′,

Reverse 1, 5′-ACGGACCCAGGCTGACTTATCTC-3′,

Reverse 2, 5′-GGCACGTGCACAGGAAATAGC-3′.

RIPK3$^{-/-}$ and wild-type (WT) mice were infected with 5×10^5 PFUs of HTNV through intravenous injection. Body weights and anal

temperatures were detected daily. At nine days postinfection (dpi), mice were anesthetized for routine blood tests and pathological assessment of the organs.

2.5. RNA extraction and quantitative real-time PCR (qRT-PCR) analysis

Total cellular RNA was extracted from cultured cells or fresh tissue samples with TRIzol (Invitrogen, 15596026), and the RNA concentration was measured using a BioTek Epoch instrument. Reverse transcription (RT) was performed with Hifair® II 1st Strand cDNA Synthesis SuperMix (Yeasen, 11120ES60) according to the manufacturer's instructions. Real-time PCR was carried out by using Hieff® qPCR SYBR Green Master Mix (Yeasen, 11201ES08) on a CFX96™ instrument (Bio-Rad, USA). The protocol was as follows: Each cDNA was denatured at 95 °C for 10 s and amplified for 40 cycles of 10 s at 95 °C and 30 s at 60 °C in a LightCycler 96 instrument (Roche, Switzerland). The mRNA expression level of each target gene was normalized to the respective GAPDH level and analyzed. The primer sequences were obtained from PrimerBank (http://pga.mgh.harvard.edu/primerbank) and are shown in Supplementary Table S3.

2.6. Immunoblot assays and coimmunoprecipitation (co-IP)

Tissue and cell lysates were prepared in RIPA lysis buffer (Beyotime, China) containing protease inhibitor cocktail (Targetmoi, USA) and phosphatase inhibitor cocktail I and II (Targetmoi, USA) for the radioimmunoprecipitation assay. The total protein concentrations were measured using a Pierce™ BCA Protein Assay Kit (Thermo, USA). Protein samples were separated by 10% SDS-PAGE and transferred to polyvinylidene fluoride (PVDF) membranes. Then, a 5% nonfat milk solution was used for blocking at room temperature (25 °C) for 1.5 h. Next, diluted primary antibody (1:1000) was added for incubation at 4 °C overnight, and secondary antibody (1:10,000) labeled with infrared dye was incubated with the membrane for 1 h at room temperature (25 °C). Signals on the PVDF membrane were visualized using the Odyssey Infrared Imaging System (LI-COR Biosciences, USA). Densitometric analysis of protein band intensity was performed by using ImageJ software (NIH, USA). GAPDH was used as a loading control for normalization. For co-IP, cells transfected with plasmids for 48 h were harvested and lysed with IP lysis buffer for 1 h. The supernatants were collected via centrifugation at 13,523 ×*g* for 20 min at 4 °C. Then, the supernatants were incubated with magnetic beads with a tag antibody overnight at 4 °C with rotation. Beads were collected and washed three times with washing buffer. Then, the beads were boiled at 100 °C for 5 min in 5× SDS protein loading buffer and analyzed by immunoblotting as mentioned above. The antibodies used are shown in Supplementary Table S4.

2.7. Absolute quantification of the viral load

The HTNV-S standard was obtained using the pcDNA 3.1-HTNV-S plasmid and an *in vitro* transcription system, and the HTNV-S copy number was calculated according to the following formula: copy number (copies/μL) = ng × 10 − 9 × 6.02 × 1023 ÷ base number ÷ 345. After gradient dilution of the standard, the Ct value was determined by qRT-PCR, and the Ct value of HTNV-S in serum was obtained. The HTNV-S copy number was calculated according to the standard curve and the formula above.

2.8. Murine sepsis score (MSS)

The severity of infection in mice was determined using variables that have been described in the literature (Shrum et al., 2014). The variables that were incorporated into the MSS (as shown in Supplementary Table S5) included appearance, autonomous consciousness, autonomous activities and response to stimulation. Each of these variables was given a score between 0 and 4. A higher number implied increased infection severity in mice. We do not present the scores taken from days 0–6 after infection because the WT and RIPK3$^{-/-}$ mice did not show phenotypic differences prior to day 7.

2.9. Hematoxylin and eosin (H&E) staining

Tissue samples (liver, lung and kidney) were preserved in 4% neutral buffered formalin for histopathological analysis. The tissues were then dehydrated, paraffin-embedded, and sectioned. The sectioned tissue slides were stained in hematoxylin solution. Images were acquired using 3DHISTECH scanners (Hungary). The tissue sections were observed in detail at different magnifications, and fundamental pathological changes in the sections, such as congestion, bleeding, edema, degeneration, necrosis, hyperplasia, fibrosis, mechanization, the presence of granulation tissue and inflammatory changes, were noted.

2.10. Immunofluorescence assay

After embedded in paraffin, the tissues were cut into 4-mm-thick sections using a microtome. After antigen repair, diluted 3% bovine serum albumin (BSA) was used for blocking. The tissues were then incubated with monoclonal antibodies against HTNV-NP, STAT1 and F4/80 overnight at 4 °C. Then, the samples were incubated with secondary antibody, followed by DAPI staining at room temperature (25 °C) for 5–10 min, and images were acquired using 3DHISTECH (Hungary) and analyzed using CaseViewer2.4.

Cells were placed on small discs in 24-well plates, fixed with 4% paraformaldehyde (PFA) (Sangon Biotech, China) at room temperature (25 °C) for 15 min and then permeabilized with 0.5% Triton X-100 (Sangon Biotech, China) for 15 min. After blocking with 3% BSA for 1 h, primary antibody at the appropriate dilution was added and incubated overnight at 4 °C. After three washes with DPBS, a fluorochrome-conjugated secondary antibody was used for detection. The cellular nuclei were stained with DAPI (Sangon Biotech, China), and all samples were observed under a laser scanning confocal microscope (FV3000, Olympus, Japan).

2.11. Transmission electron microscopy (TEM) assay

Tissue samples (lungs) were sectioned into 1 × 1 × 3 mm^3 pieces and immediately soaked in a glutaraldehyde fixation solution at a volume no less than 40 times the tissue volume. The air was removed using a syringe until the lung tissue was entirely below the fluid level. The treated tissues were block mounted and thinly sectioned (Leica, China). The sections were first stained with uranyl acetate for 30 min and rinsed 3–5 times with double-distilled water. The sections were then stained with lead citrate for 10 min. They were photographed using a Hitachi HT7700 transmission electron microscope (Hitachi, Japan), and the images were processed with a Hitachi TEM system. The experiment was supported by on-campus technology (Wang et al., 2019).

2.12. Dual-luciferase assays

The plasmids pGL3-Basic, IRES-Luc and STAT1-Luc were stored in our laboratory; the reporter plasmids for IFN-Luc were purchased from Miaoling Biology. HEK293T cells in 24-well plates were transfected with different luciferase plasmids (100 ng), pRL-TK (10 ng), and other desired plasmids (400 ng) in each well by Hieff trans™ liposomal transfection reagent (Yeasen, China) and then stimulated with or without poly(I:C) (MedChemExpress, USA). After lying the cells, the Renilla and firefly luciferase activities were measured using the dual-luciferase assay system (Promega, USA).

2.13. Flow cytometry for Annexin V-propidium iodide (PI) staining

Cells were digested and collected in a centrifuge tube, washed with DPBS twice and centrifuged at 94 × *g* at room temperature (25 °C) for 3 min. For cell staining, an Annexin V-PI staining kit (BD, USA) was used according to the manufacturer's instructions. Annexin V (5 μL) and PI (5 μL) were added, and the volume was brought to 1 mL with 1× binding buffer. The samples were incubated at room temperature (25 °C) for 15–20 min without light exposure. Stained cells were analyzed in a FACSCanto II flow cytometer (BD, USA) within 1 h.

2.14. ATP production assay

ATP production in BMDMs was measured using an ATP assay kit (Beyotime, China) as previously described (Li et al., 2020). The supernatant of the cells was collected. Then, ATP detection solution (100 μL) was added to 96-well plates. Five minutes later, 50 μL of the sample was added, and the relative light unit value was detected on a microplate reader.

2.15. Calcein/PI cell viability assay

An appropriate volume of Calcein AM/PI working solution was added (usually 50 μL for each well of a 96-well plate). After incubation at 37 °C for 30 min away from light, staining was observed under a fluorescence microscope (Calcein AM was identified by green fluorescence, Ex/Em = 494/517 nm; PI was identified by red fluorescence, Ex/Em = 535/617 nm). ImageJ was used to calculate the cell number, and at least three visual fields for all samples were assessed (Calcein/PI Cell Viability/Cytotoxicity Assay Kit, Beyotime).

2.16. Enzyme-linked immunosorbent assay (ELISA)

The concentrations of mouse IFN-α/β in the cell supernatants were evaluated with a QuantiCyto® mouse IFN-α/β ELISA kit according to the manufacturer's instructions. In short, standard samples were prepared at a gradient dilution to prepare a standard curve. The samples were diluted with specific buffer, added to a plate precoated with anti-cytokine antibodies, and then reacted with HRP-conjugated detection antibodies. TMB and stop solution were added sequentially, and then the OD450 was measured within 30 min. The cytokine concentration was calculated according to the standard curve.

2.17. Protein docking

The protein structures were downloaded from uniport (https://www.uniprot.org). The identifier of RIPK3 is AF-Q9QZL0-F1, and the identifier of STAT1 is AF-P42225-F1. The HDOCK server, Protein-Ligand Interaction Profiler (PLIP) and Protein Database Summaries (PDBsum) database were used to predict protein interactions. HDOCK provides two indicators, namely, the docking score and confidence score. A lower docking score indicates a more likely combinational model, while a confidence score higher than 0.7 suggests a possible interaction (Yan et al., 2017). The docking score for our model (RIPK3-STAT1) was −240.13, and the confidence score was 0.8585. The PDBsum database provides a graphical outline of the proteins (Laskowski, 2001). PLIP is an analytical tool for the noncovalent interactions of protein ligands. It can analyze the noncovalent interactions of paired complexes at the atomic level, including hydrophobic interactions, hydrogen bonds, and salt bridges (Salentin et al., 2015).

2.18. Quantification and statistical analysis

Statistical analysis was performed by GraphPad Prism 9 software. Data are representative of three independent experiments and are expressed as the mean ± standard error of the mean (SEM) for *in vitro* data or ± SD for *in vivo* data. Student's *t*-test or one-way analysis of variance (ANOVA) was used to assess the significance of differences between groups. (*$P < 0.05$; **$P < 0.01$; ***$P < 0.001$; ns, no significance).

3. Results

3.1. HTNV infection enhanced the expression of necroptosis-associated genes without triggering cell death

Programmed cell death (PCD), which includes apoptosis, necroptosis and pyroptosis, is a form of host defense against viral infection (Nguyen and Kanneganti, 2022). However, the relationship between cell death and HTNV infection is still unclear. Unlike JEV, which elicits cell death facilitating neuroinflammation and viral propagation, HTNV fails to induce a classic cytopathic effect (CPE), with the mechanisms unidentified (Bian et al., 2020; Yiang et al., 2013). Kyoto Encyclopedia of Genes and Genomes (KEGG) pathway enrichment analysis was performed with our RNA-seq data, and the results revealed that several cell death-associated pathways were strongly associated with HTNV and JEV infection (Fig. 1A). Notably, the expression of most apoptosis- and necroptosis-related genes was upregulated at 36 h after HTNV infection, differing from the tendency of these genes to be downregulated in the JEV infection groups (Fig. 1B). To assess changes in these genes, qRT-PCR was performed at specific time points after infection. We found that expression of the necroptosis-associated gene, *Ripk3,* was significantly enhanced in the late HTNV infection phase, while *Mlkl* expression was increased at 12 hpi but had returned to baseline at 36 hpi (Fig. 1C). Immunoblot assays confirmed the increased expression of RIPK3 but not p-MLKL (Ser345) (Fig. 1D, Supplementary Fig. S1A). These results showed that HTNV infection enhanced the expression of necroptosis-associated genes, but whether cell death had been induced remained unclear. Consistent with previous studies (Hardestam et al., 2005; Solà-Riera et al., 2020), the results of both ATP detection (Fig. 1E) and PI staining (Fig. 1F, Supplementary Fig. S1B) implied that, unlike JEV, HTNV could not trigger cell death from 0 to 48 hpi. These observations indicated that necroptosis-associated proteins might play a noncanonical role without causing cell death during HTNV infection.

To investigate whether HTNV-infected cells are resistant to necroptosis, classic TSZ (TNF-α, smac mimetic and zVAD-fmk) treatments were applied to induce a necrotic morphology (Weigert et al., 2017). Flow cytometry showed that TSZ efficiently induced cell death in L929 cells but not A549 cells (Supplementary Fig. S1C) (Zhan et al., 2022). However, HTNV infection did not affect TSZ-induced MLKL activation (Fig. 1G, Supplementary Fig. S1D). In addition, an ATP production assay showed that HTNV infection could not reverse the reduction in ATP levels induced by TSZ at 6 or 12 h (Fig. 1H). The cell morphology was observed under a microscope at 6 h after TSZ stimulation. HTNV could not prevent the cells from shrinking and rounding (Fig. 1I). These results demonstrated that HTNV neither induced necroptosis nor antagonized TSZ-induced cell death.

3.2. RIPK3 facilitated HTNV replication by intercepting STAT1-mediated antiviral responses

To explore the potential role of necroptosis-associated proteins in virus infection, we silenced these proteins with RNAi assays, and then the HTNV replication level was measured by immunoblotting and qRT-PCR. Downregulation of MLKL did not decrease HTNV NP expression or HTNV S segment transcription (Supplementary Fig. S2A and Fig. 2A). Knocking down Z-DNA binding protein 1 (ZBP-1), which can trigger IFN production and necroptosis as a PRR against viral infection (Koehler et al., 2021), promoted HTNV replication, while silencing RIPK3 restrained viral protein and RNA generation (Supplementary Fig. S2A and Fig. 2A). Additionally, HTNV NP and S segment expression was also enhanced in

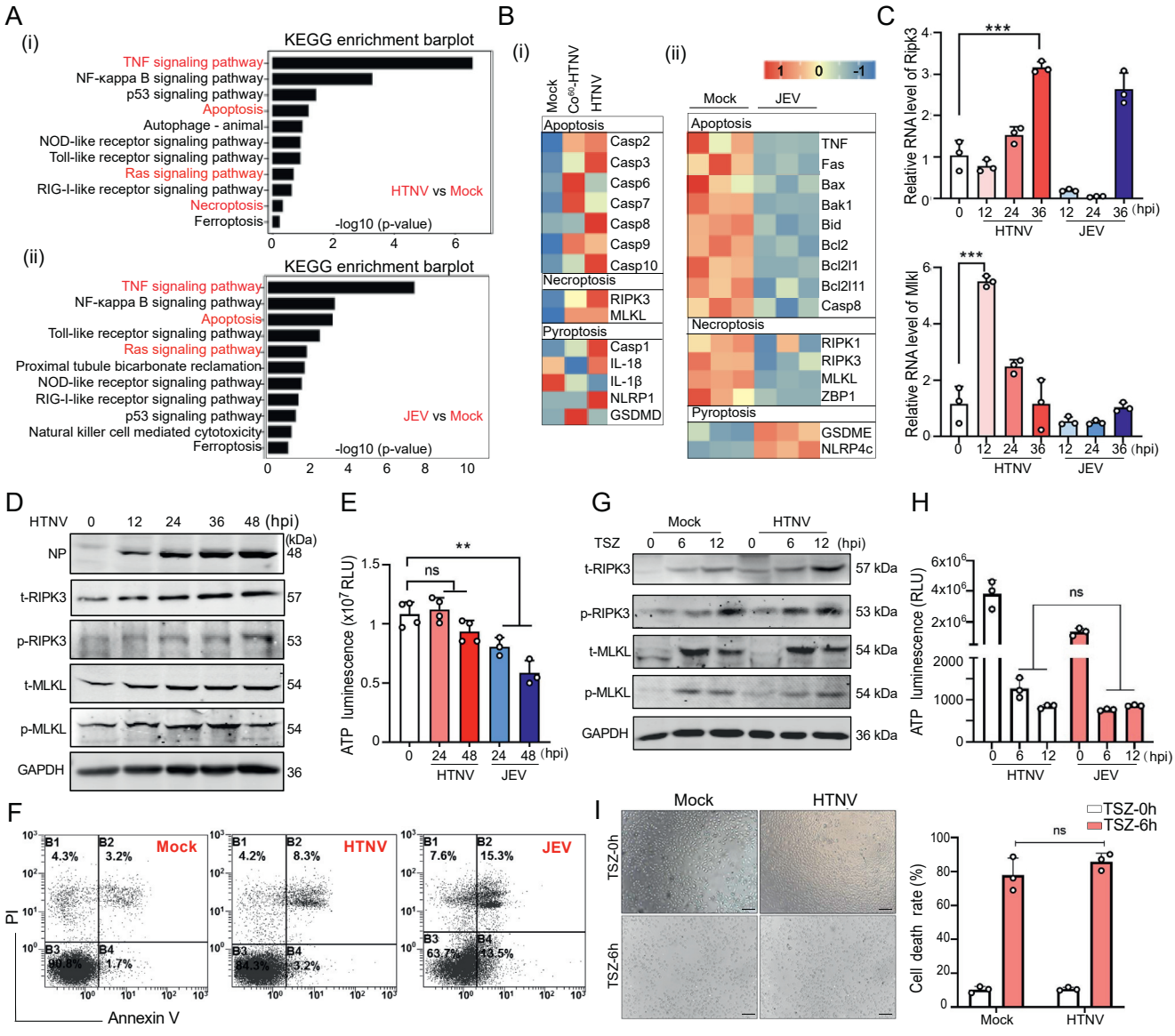

Fig. 1. HTNV infection enhanced the expression of *Ripk3* and other necroptosis-associated genes without triggering cell death. **A** KEGG analysis showing the cell death-associated pathways enriched in HTNV-infected HUVECs (i) and JEV-infected Neuro-2a cells (ii). **B** Heatmaps showing the genes involved in the enrichment of cell death-associated pathways (apoptosis, necroptosis, pyroptosis and ferroptosis) in Co^{60}-HTNV (inactivated HTNV under irradiation by Co^{60})/HTNV-infected HUVECs (i), and JEV-infected Neuro-2a cells (ii). The two datasets were derived from our previous studies (Bian et al., 2020; Yang et al., 2022). **C** The mRNA levels of necroptosis-associated molecules were measured by qRT-PCR in BMDMs that were infected with HTNV or JEV, respectively (MOI = 1). **D** Protein levels of necroptosis-associated molecules were measured by immunoblotting in HTNV-infected BMDMs (MOI = 1). **E** Representative ATP luminescence assays from independent experiments that measured the growth of indicated cells. The ATP was released intracellularly by BMDMs infected with either HTNV or JEV. **F** BMDMs infected with HTNV or JEV for 36 h (MOI = 1) were stained with Annexin V and Propidium Iodide (PI) and analyzed by flow cytometry. The X and Y axes represent Annexin V and PI staining, respectively. **G**, **H** and **I** L929 cells were pretreated with tumor necrosis factor α (TNF-α), a smac mimetic and zVAD-fmk (TSZ) for 6 h and then infected with HTNV at an MOI of 1 for 24 h (T: TNF, 10 ng/mL; S: Smac mimetic (SM-164), 100 nmol/L; Z: zVAD-fmk, 20 μmol/L). The expression of necroptosis-associated molecules was evaluated by immunoblotting (**G**). The luminescence values indicating ATP release are shown in (**H**). Representative microscopic images show the cell morphology under different treatments, and histograms show the percentage of round cells under different views (**I**), Scale bar = 100 μm. Data represent the means ± SEM. $^{*}P < 0.05$, $^{**}P < 0.01$, and $^{***}P < 0.001$.

$RIPK3^{-/-}$ BMDMs (Fig. 2B and Supplementary S2B). Consistently, overexpressing RIPK3 facilitated HTNV replication (Fig. 2C and Supplementary S2C).

Our previous results indicated that RIPK3 serves as a negative regulator of ISGs and promotes JEV replication (Bian et al., 2020). However, it was unclear whether RIPK3 regulates IFN responses during HTNV infection. RNA-seq was performed to compare the gene expression profiles of WT and RIPK3 knockout ($RIPK3^{-/-}$) BMDMs at 24 hpi (Fig. 2D-i). Principal component analysis (PCA) indicated strong consistency among the three replicates of each group (Fig. 2D-ii). Differentially expressed genes are presented in a volcano plot; of these genes, 133 genes were significantly downregulated (blue plots), while 636 genes (orange plots, including several classic ISGs such as *Mx1*, *Mx2* and *Isg15*) were upregulated in the RIPK3 knockout group (Fig. 2D-iii). KEGG pathway enrichment analysis revealed that PRR signaling (NOD-like, RIG-I-like and TLR-like receptor signaling) and the JAK-STAT pathway were significantly enriched in HTNV-infected $RIPK3^{-/-}$ BMDMs compared with WT BMDMs (Fig. 2E-i). Transcription levels of a series of

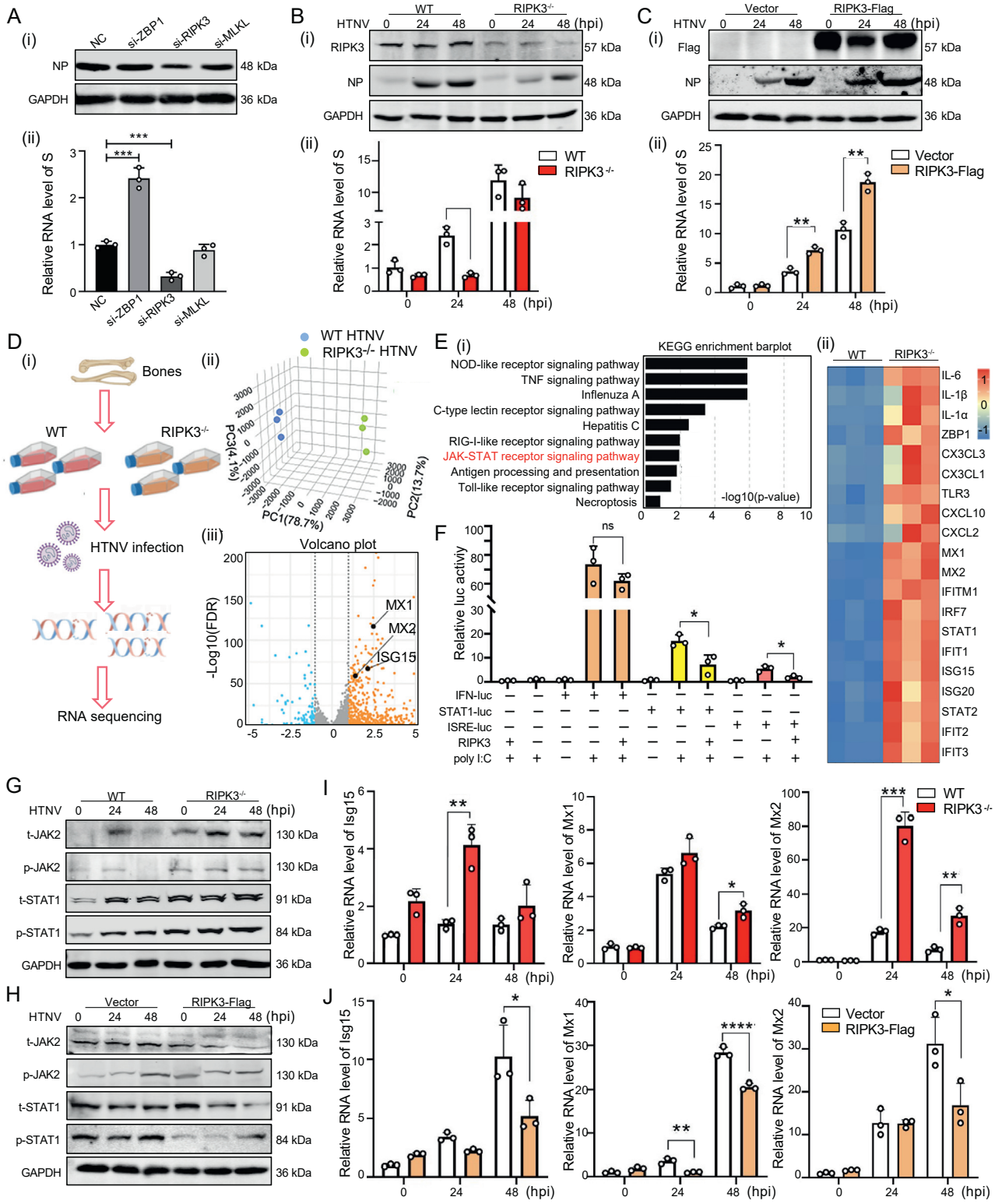

(caption on next page)

Fig. 2. RIPK3 facilitated HTNV replication by intercepting STAT1-mediated antiviral responses. **A** BMDMs were transfected with different siRNAs (NC, si-ZBP1, si-RIPK3, and si-MLKL) and then infected with HTNV for 24 h (MOI = 1). The protein levels (i) and RNA levels (ii) of the NP of HTNV were measured by immunoblotting and qRT-PCR, respectively (S is a segment of the genome of HTNV encoding NP). **B** RIPK3$^{-/-}$ BMDMs were infected with HTNV (MOI = 1), and the cell lysates were then collected to analyze NP levels using immunoblotting (i) and HTNV-S levels using qRT–PCR (ii). **C** Huh-7 cells were transfected with the RIPK3-Flag plasmid for 24 h and infected with HTNV (MOI = 1). Cell lysates were then collected for the analysis of viral NP levels using immunoblotting (i), and viral RNA levels using qRT-PCR (ii). **D** WT/RIPK3$^{-/-}$ BMDMs were isolated from the bones of WT/RIPK3$^{-/-}$ C57BL/6J mice, and then infected with HTNV for 24 h (MOI = 1). RNA was then extracted for RNA sequencing, as shown in a flowchart (i). Principal component analysis demonstrated the total variance in two major principal components (92.4%) (ii). A Volcano plot shows the up- and downregulated transcripts determined by RNA sequencing of BMDMs (iii). **E** KEGG analysis revealed immune-associated pathways enriched in the samples in (**D**) (i). A heatmap shows the enriched genes encoding inflammatory cytokines and IFN-associated cytokines (ii). **F** HEK293T cells transfected with the RIPK3 plasmid and IFN/STAT1/ISRE reporter plasmids were stimulated by poly(I:C). Reporter assays were performed 24 h after poly(I:C) stimulation. **G** RIPK3$^{-/-}$ BMDMs were infected with HTNV (MOI = 1), and the cell lysates were then collected to analyze the JAK-STAT pathway indicators by immunoblotting. **H** Huh-7 cells were transfected with the RIPK3-Flag plasmid and infected with HTNV (MOI = 1). The cell lysates were detected with the same indicators of (**G**) by immunoblotting. **I** The cell lysates of (**G**) were collected to analyze ISGs using qRT-PCR. **J** The cell lysates of (**H**) were collected to analyze ISGs using qRT-PCR. Data represent the mean ± SEM. $^{*}P < 0.05$, $^{**}P < 0.01$, and $^{***}P < 0.001$.

proinflammatory genes (including *Il-6* and *Il-1*) and antiviral ISGs (e.g., *Ifit1*, *Ifit2,* and *Ifitm1*) were remarkably upregulated in the RIPK3 knockout group (Fig. 2E-ii). To investigate how RIPK3 modulates the IFN pathway, the JAK/STAT pathway and PRR signaling activation were first assessed during the natural HTNV infection process. Immunoblot analysis suggested that STAT1 phosphorylation was significantly increased at 24 hpi and then maintained at a relatively low level from 36 to 48 hpi, during which JAK2 was obviously activated (Supplementary Fig. S2D). These data indicated that HTNV might restrict the activation of STAT1 but not JAK2 at the late infection phase (from 36 to 48 hpi). Concurrently, the expression of PRRs (including TLR3 and TLR4) and the production of IFNs and ISGs were enhanced from 0 to 48 hpi during HTNV infection (Supplementary Fig. S2E). Next, we assessed how RIPK3 inhibits IFN signaling using plasmids containing different luciferase reporter genes. We found that overexpressing RIPK3 remarkably suppressed STAT1-and ISRE-driven luciferase activity after poly(I:C) stimulation but did not affect IFN-driven luciferase activity (Fig. 2F). Consistently, there was no differences in IFN-α or IFN-β secretion between WT and RIPK3$^{-/-}$ BMDMs after HTNV infection (Supplementary Fig. S3A). Notably, RIPK3 knockout promoted the expression of STAT1 and its phosphorylation (Ser727) at 48 hpi (Fig. 2G and Supplementary Fig. S3B), and RIPK3 overexpression inhibited STAT1 activation from 0 to 48 hpi (Fig. 2H and Supplementary Fig. S3C). The expression levels of multiple ISGs were also increased in RIPK3$^{-/-}$ BMDMs (Fig. 2I and Supplementary Fig. S3D) and downregulated in the RIPK3 overexpression group (Fig. 2J and Supplementary Fig. S3E).

Additionally, RIPK3 knockout restrained the expression of *Il-10 and Arg-1*, which are markers of alternative macrophage activation (M2) (Gordon and Martinez, 2010), but enhanced the expression of *Il-1β* and *Il-6 at* 48 hpi (Supplementary Fig. S3F), indicating that RIPK3$^{-/-}$ BMDMs exhibited a proinflammatory phenotype in the late infection phase. In brief, RIPK3 could facilitate HTNV replication by restricting STAT1-mediated antiviral responses.

3.3. RIPK3 interacted with STAT1 and inhibited its phosphorylation during HTNV infection

To clarify how RIPK3 affected STAT1 activation, their subcellular locations were detected through immunofluorescence assays. Intriguingly, the subcellular localization of STAT1 was altered following HTNV infection or RIPK3 overexpression, which means that STAT1 is usually scattered in the cytoplasm but was recruited from the cytoplasm of the cell to the periphery of the nucleus and colocalized with RIPK3 (Fig. 3A and B). We hypothesized that RIPK3 might directly interact with and sequester STAT1 in the perinuclear endoplasmic reticulum. As expected, overexpressed RIPK3 with a Flag tag (RIPK3-Flag) could pull down Myc-tagged STAT1 (STAT1-Myc) (Fig. 3C), and RIPK3-Flag could also be coimmunoprecipitated with STAT1-Myc (Fig. 3D). Notably, RIPK3 hindered the translocation of STAT1 from the cytoplasm to the nucleus. To clarify whether HTNV infection can strengthen this interaction, we conducted endogenous co-IP of RIPK3 and STAT1 from HTNV-infected BMDMs, and the level of STAT1 was significantly enriched by RIPK3 after HTNV infection (Fig. 3E).

To further investigate how RIPK3 targets and inactivates STAT1, further bioinformatic analysis and co-IP assays were performed. Molecular docking analysis indicated that multiple amino acid residues in the PKD of RIPK3 (e.g., Glu2, Gln108, Val228, and Thr248) could interact with STAT1 (Fig. 3F and G). Hence, truncation plasmids of RIPK3 (ΔPKD and ΔRHIM) were constructed (Fig. 3H-i). As expected, ΔRHIM but not ΔPKD RIPK3 could be pulled down by STAT1 (Fig. 3H-ii), demonstrating that the PKD of RIPK3 mediates its interaction with STAT1. Next, we asked whether the kinase activity of RIPK3 determines the STAT1 inactivation process. To address this issue, point mutants of RIPK3 (K51A and D161N) were constructed to inactivate its kinase domain (Newton et al., 2014; Zhao et al., 2017). Overexpressing either RIPK3(K51A) or RIPK3(D161N) inhibited HTNV-induced STAT1 phosphorylation, thus promoting HTNV replication (Fig. 3I). These data indicated that PKD of RIPK3 interacts with STAT1, and hinders its activity independent of RIPK3's kinase activity.

3.4. RIPK3-deficient mice showed mild clinical symptoms and limited pathological alterations after HTNV infection

Although previous results showed that RIPK3 could inactivate STAT1 and facilitate HTNV replication *in vitro*, it was still unclear whether this regulatory process would occur *in vivo*. RIPK3$^{-/-}$ mice were challenged with HTNV (Fig. 4A) and monitored daily for clinical symptoms, body weight, and temperature alteration postinfection. Previous studies have noted that RIPK3$^{-/-}$ mice develop normally with no histological defects in their major organs (Dermentzaki et al., 2019; Hansen et al., 2018), and we also found that there was no pathological alteration of the organs or phenotypic difference between uninfected WT and RIPK3$^{-/-}$ mice (Supplementary Fig. S4A–S4C). In contrast, unlike the infected WT mice, the infected RIPK3$^{-/-}$ mice showed mild clinical symptoms, such as ruffled fur and sluggish movement (Fig. 4B). The MSS is typically used to assess the severity of sepsis in mice based on observational characteristics (Sulzbacher et al., 2022). We found that RIPK3$^{-/-}$ mice showed sepsis-like symptoms with higher MSS scores from 7 to 9 dpi (Fig. 4C). Regarding weight change, RIPK3$^{-/-}$ mice gained weight more slowly than the WT mice after HTNV infection (Fig. 4D). Moreover, the body surface temperature in the head, back or tail (Fig. 4E, Supplementary Fig. S4D and Supplementary Table S6), as well as the core temperature assessed through the anus (Fig. 4F), were significantly higher in RIPK3$^{-/-}$ mice from 7 to 9 dpi. Laboratory parameters generally used in the clinic were measured. Most of the peripheral immune cells, including neutrophils and lymphocytes but not monocytes, were mobilized in the HTNV-infected RIPK3$^{-/-}$ mice (Fig. 4G). Notably, the reduction in blood platelet (PLT) counts, which indicate HFRS disease severity, was reversed in HTNV-infected RIPK3$^{-/-}$ mice (Fig. 4G). However, serological tests for liver and kidney function revealed no substantial organ damage in HTNV-infected RIPK3$^{-/-}$ mice, suggesting that their disease symptoms were self-limited and controllable (Fig. 4H and Supplementary Fig. S4E).

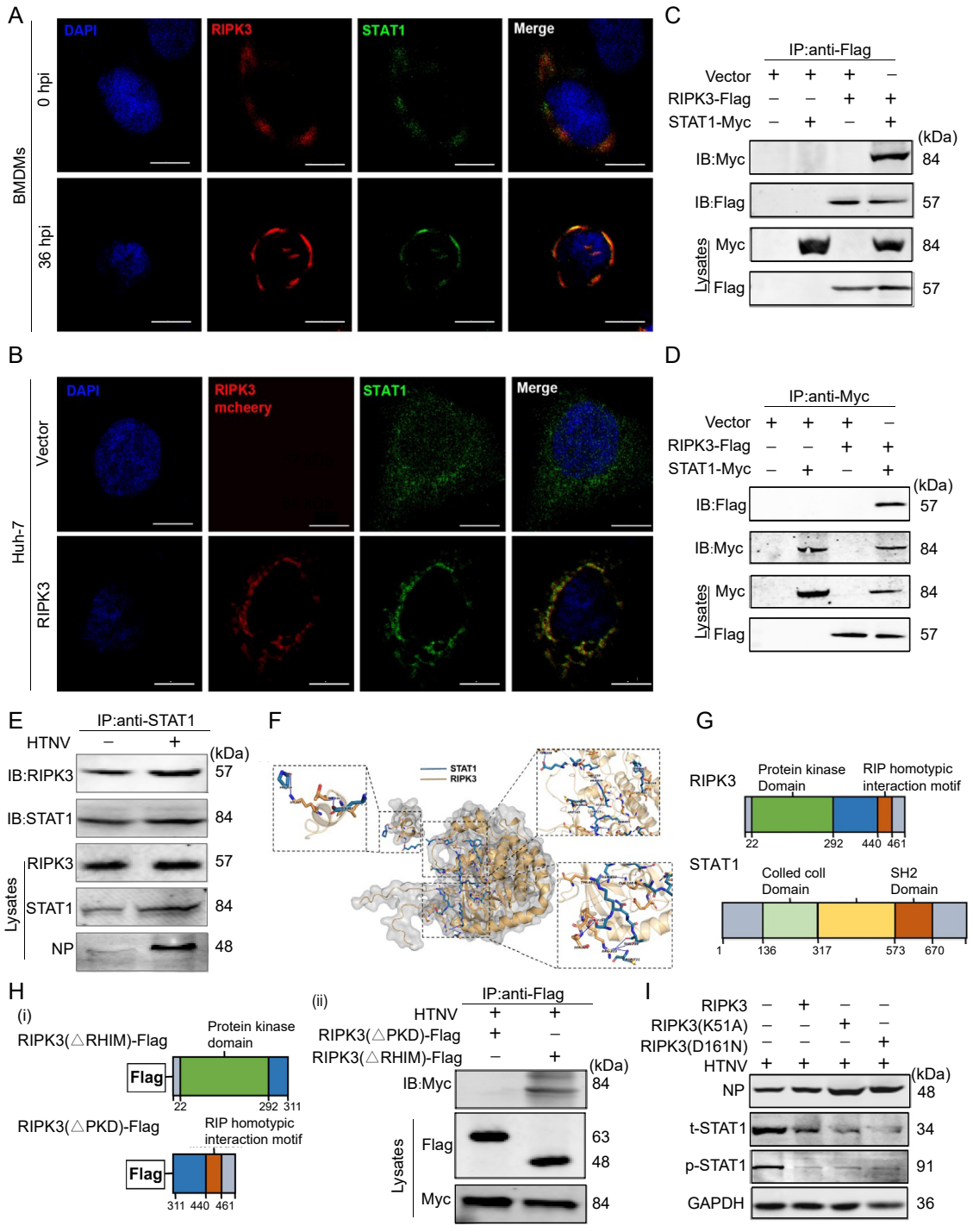

Fig. 3. RIPK3 interacted with STAT1 and inhibited its phosphorylation during HTNV infection. **A** BMDMs were infected with HTNV (MOI = 1) for different durations, and then an immunofluorescence assay was conducted to evaluate endogenous levels of RIPK3 (red) and STAT1 (green). Scale bar, 5 μm. **B** HTNV-infected Huh-7 cells were transfected with the relevant plasmid (vector/pCMV-RIPK3-mCherry) and then underwent immunofluorescence assays (IFAs) to mark exogenous RIPK3 (red) and STAT1 (green). Scale bar, 5 μm. (**C** and **D**) RIPK3-Flag was coexpressed with STAT1-Myc in HEK293T cells. Cell lysates were subjected to co-IP and analyzed via immunoblotting. **E** BMDMs were previously infected with HTNV at 24 h (MOI = 1). The interactions between endogenous RIPK3 and STAT1 in cell lysates were analyzed using co-IP and immunoblotting. Top panel (STAT1 IP'ed samples): immunoblots containing RIPK3 and STAT1 proteins. Bottom panel (Input): immunoblots containing total protein extracts. **F** Detailed interacting amino acid residues were determined by PLIP. RIPK3 (yellow) was used as the target protein. **G** A schematic representation of the RIPK3 and STAT1 architecture is shown. The colored boxes show different functional domains. **H** A schematic representation of RIPK3ΔPKD-Flag and RIPK3ΔRHIM-Flag is shown (i). RIPK3ΔPKD-Flag or RIPK3ΔRHIM-Flag was coexpressed with STAT1-Myc in HEK293T cells. Cell lysates were subjected to co-IP and analyzed via immunoblotting. Top panel (Myc IP'ed samples): immunoblots containing STAT1-Myc proteins. Bottom panel (Input): immunoblots containing total protein extracts. Co-IP assays showed that deletion of protein kinase domain in RIPK3 (ΔPKD) could interact with STAT1, whereas ΔRHIM did not. **I** Huh-7 cells were transfected with the appropriate plasmid to express RIPK3/RIPK3(K51A)/RIPK3(D161N) and then infected with HTNV for 24 h (MOI = 1). Cell lysates were then collected to analyze STAT1 activation using immunoblotting. The data are the means ± SEMs. $^{*}P < 0.05$, $^{**}P < 0.01$, and $^{***}P < 0.001$.

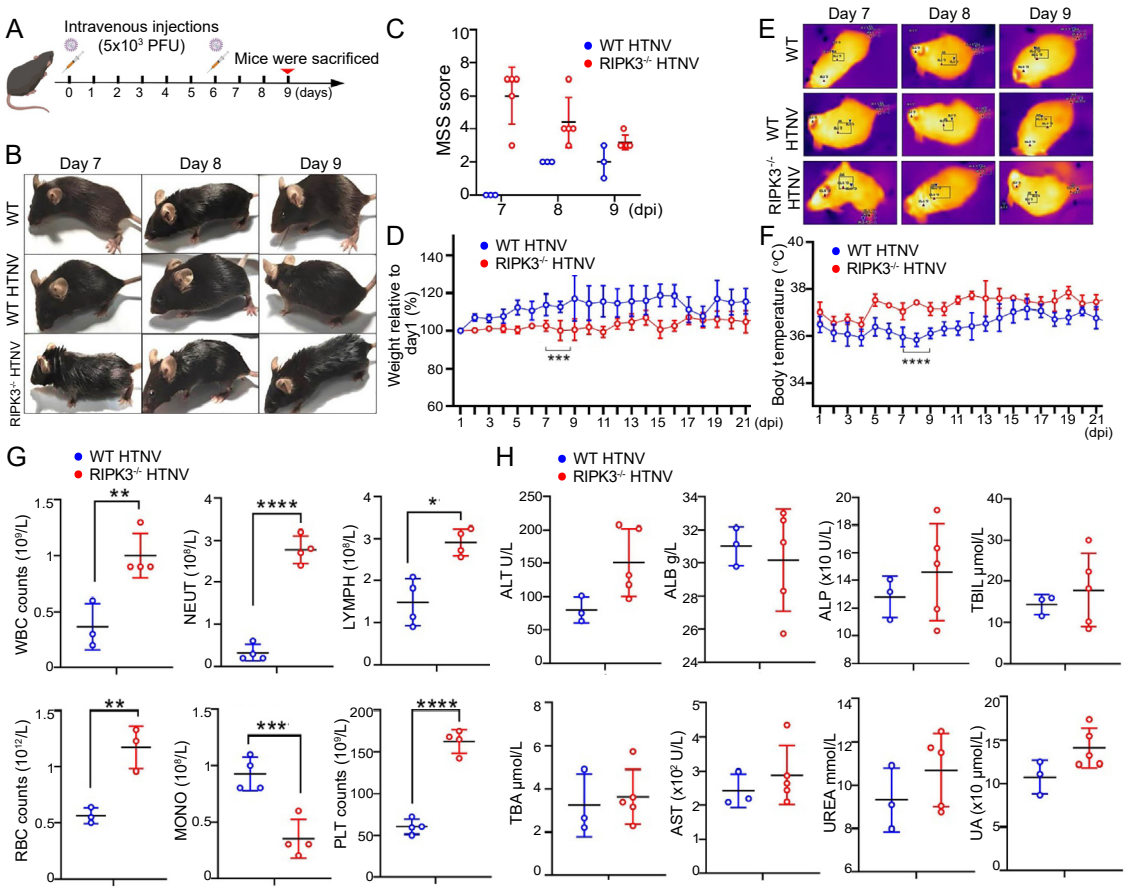

Fig. 4. RIPK3-deficient mice showed mild clinical symptoms and limited pathological alterations after HTNV infection. **A** Schematic showing the experimental steps for virus challenge of WT/RIPK3$^{-/-}$ mice with 5 × 10^5 PFUs of HTNV 76-118. On day six, we conducted the second HTNV infection challenge at the same dose. On day nine, mice were anesthetized and euthanized for routine blood tests and pathological assessment of the organs. **B** Pictures show the clinical symptoms of WT/RIPK3$^{-/-}$ mice from day 7–9 after virus challenge. **C** The murine clinical score (MSS) was recorded from day 7–9 after virus challenge. A higher number implied increased infection severity in mice. **D** The body weights of WT/RIPK3$^{-/-}$ mice were recorded daily after infection. **E** Images showing the core temperature of WT/RIPK3$^{-/-}$ mice from day 7–9 days after virus challenge, with data collected from the head, back and tail. **F** Body temperature of WT/RIPK3$^{-/-}$ mice was recorded daily after infection. **G** and **H** Hematological examination of WT/RIPK3$^{-/-}$ mice after infection. Whole blood was collected on day 9 after infection for routine blood tests (**G**). The whole blood was centrifuged at 1500 ×*g* for 10 min at room temperature (25°C) to obtain serum for biochemical tests (**H**). Data represent mean ± SD. *$P < 0.05$, **$P < 0.01$, and ***$P < 0.001$.

These results suggested that RIPK3$^{-/-}$ mice exhibited mild clinical symptoms during HTNV infection.

3.5. *RIPK3-deficient mice maintained prompt HTNV clearance with enhanced inflammatory responses*

To investigate the dissemination and replication of HTNV in virus-challenged mice, HTNV RNA was extracted from serum to determine viral replication in the blood at 9 dpi (Fig. 5A). The viral copy number in the RIPK3$^{-/-}$ mice was clearly lower than that in the WT mice (RIPK3$^{-/-}$ mice: 683.7 ± 305.5 copies per μL; WT mice: 1613 ± 273.1 copies per μL). In addition, the protein expression of HTNV-NP in the major organs (including the lung, spleen and kidney) was significantly suppressed in RIPK3$^{-/-}$ mice (Fig. 5B). Pathological changes in the HTNV-infected mice were evaluated by H&E staining. Granulocyte and macrophage infiltration in the alveoli was found in the lungs of all infected RIPK3$^{-/-}$ mice (Fig. 5C). The clinical signs caused by HTNV mainly include kidney injury characterized by acute tubulointerstitial nephritis involving the infiltration of inflammatory cells (Ma et al., 2021). However, pathological manifestations were not apparent in the liver or kidneys of HTNV-infected RIPK3$^{-/-}$ mice (Fig. 5C). Tissue immunofluorescence staining confirmed that more F4/80$^+$ macrophages infiltrated the alveoli in the RIPK3$^{-/-}$ mice after HTNV infection, which maintained lower HTNV NP production (Fig. 5D). Pathological alterations in the RIPK3$^{-/-}$ mouse lungs after HTNV infection were also confirmed by TEM, which showed increased macrophage infiltration (blue arrow), lamellar bodies (red arrow) and fibrosis (green arrow) (Fig. 5E). Collectively, these results indicated that RIPK3$^{-/-}$ mice could promptly eradicate HTNV with robust immune responses.

3.6. *RIPK3-deficient mice could efficiently launch STAT1-mediated antiviral responses against HTNV infection*

Although cell-based experiments revealed that RIPK3 modulated STAT1 to regulate HTNV replication, its function *in vivo* remained unclear. To address this question, we evaluated the activation of STAT1 in several organs. As expected, RIPK3$^{-/-}$ mice showed considerably higher STAT1 and p-STAT1 (Ser727) levels in the lungs and spleen (Fig. 6A). Additionally, tissue immunofluorescence staining showed a higher proportion of STAT1-positive cells in the lungs of RIPK3$^{-/-}$ mice (Fig. 6B). To evaluate ISG expression levels, we collected RNA from the lungs and spleen for qRT-PCR analysis. The results showed that HTNV infection significantly upregulated the expression of Mx1, Mx2, IFIT1 and ISG15 in RIPK3$^{-/-}$ mice but did not affect the expression of TLR3 or TLR4, PRRs that have been reported to be triggered by HTNV (Fig. 6C and Supplementary Fig. S4F) (Handke et al., 2009). These results indicated that

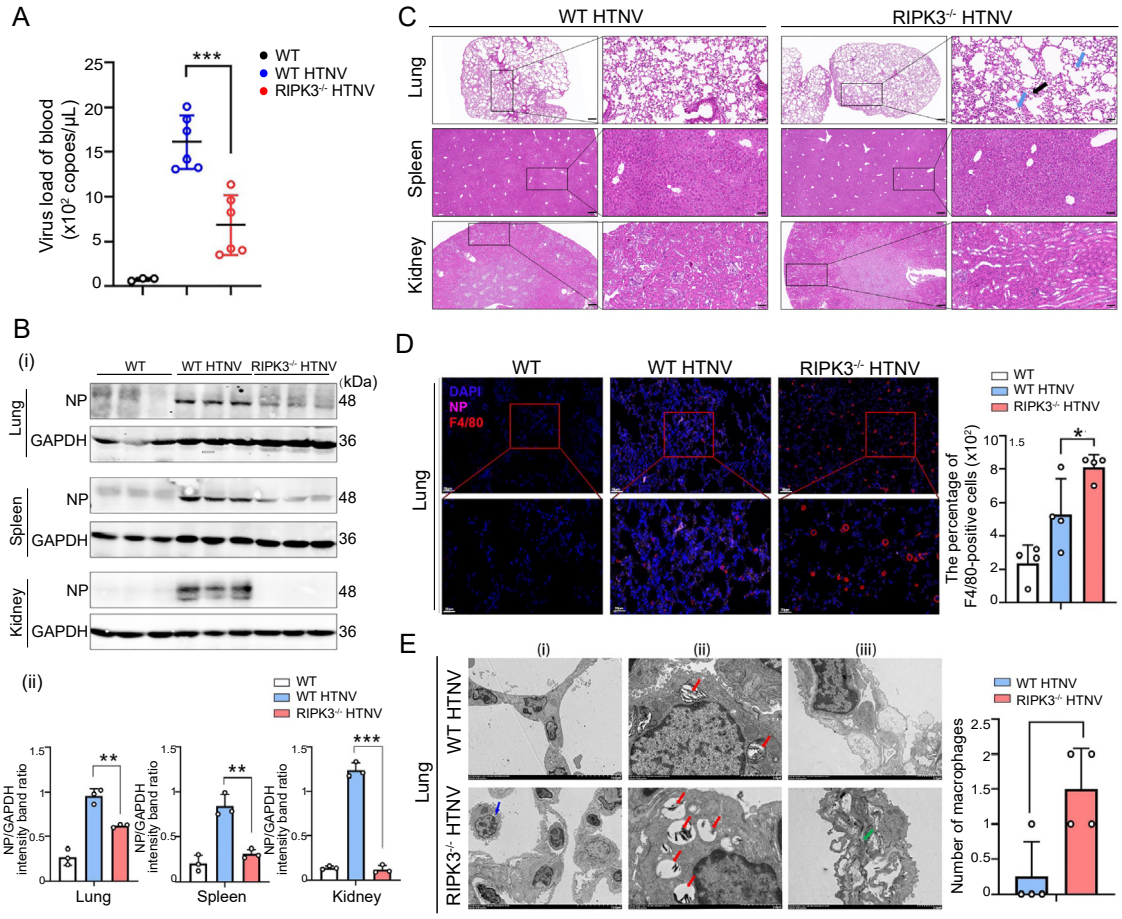

Fig. 5. RIPK3-deficient mice maintained prompt HTNV clearance capacity with enhanced inflammatory responses. **A** Whole blood was collected in EDTA anticoagulation tubes at 9 dpi. Viral loads in the plasma were quantitated by qRT-PCR. **B** Expression levels of HTNV NP in lung, spleen, and kidney samples obtained from WT and RIPK3$^{-/-}$ mice after viral challenge. Samples were collected at 9 dpi for immunoblotting (i). Densitometric analysis of band intensity for NP was performed (ii). **C** The lungs, spleen, and kidneys were collected at 9 dpi, fixed in 4% paraformaldehyde and subjected to H&E staining. Pathological analysis showed granulocyte (black arrow) and macrophage (blue arrow) infiltration in the alveoli of HTNV-infected RIPK3$^{-/-}$ mice at 9 dpi. Scale bars, 50 μm and 200 μm. **D** Tissue immunofluorescence assay in the lungs of WT/RIPK3$^{-/-}$ mice after infection. HTNV NP (pink), F4/80 (red), and DAPI (blue). Immunofluorescence images are representative of at least three samples. We used ImageJ to measure the fluorescence intensity. After detecting the fluorescence area in the picture, we calculated the ratio of the red area (F4/80) to the blue area (DAPI) and show the percentage of F4/80-positive cells in this picture. Scale bars, 50 μm and 20 μm. **E** Transmission electron microscopy was used to evaluate the lungs of WT and RIPK3$^{-/-}$ mice post-infection. In RIPK3$^{-/-}$ mice, macrophage infiltration in the alveoli (blue arrow) is shown; scale bars, 10 μm (i). The lamellar bodies of alveolar type II epithelial cells showed signs of emptying (red); scale bars, 2 μm (ii). Partial fibrosis of the alveolar wall is shown (green); scale bars, 2 μm (iii). The data are the means ± SD. *$P < 0.05$, **$P < 0.01$, and ***$P < 0.001$.

RIPK3-deficient mice showed distinct roles in clearing HTNV and promoting inflammation by regulating STAT1 activation and ISG expression.

4. Discussion

Hantaviruses can cause two kinds of viral hemorrhagic diseases in humans, namely, HFRS and hantavirus pulmonary syndrome (HPS). HTNV, the prototype hantavirus, causes severe HFRS in Eurasia and has evolved various strategies to escape the host IFN response (Ma et al., 2017a, 2017b). Previous studies suggested that HTNV and other pathogenic hantaviruses could prohibit IFN generation by degrading or inactivating MAVS, TBK1 or IRF3, providing a beneficial environment at the early infection phase (Raftery et al., 2018; Steere et al., 1987; Zhang et al., 2021). However, it was unclear how HTNV confronts IFN responses at the late infection stage. In this study, we found that HTNV infection activated RIPK3 without triggering necroptosis, especially from 24 to 48 hpi. Both *in vitro* and *in vivo*, RIPK3 promoted HTNV replication by restricting ISG expression but not by affecting IFN production. Moreover, RIPK3 targeted STAT1 and blocked its phosphorylation during HTNV infection, which was independent of the kinase activity of RIPK3 (Fig. 7).

RIPK3 is a key molecule in regulating cell death, inflammasome formation and inflammatory damage (Christgen et al., 2022; Yin et al., 2022). In the current study, we have identified novel roles for RIPK3 in the regulation of IFN signaling pathways. Knockdown of RIPK3 in BMDMs led to increased antiviral ISG production and decreased HTNV loads, and RIPK3$^{-/-}$ mice were more resistant to HTNV infection than WT mice. Although we identified RIPK3 as an important negative regulator of STAT1 during HTNV infection, at least three main questions regarding the process of HTNV infection remain: (1) what is the upstream mechanism that regulated RIPK3 expression after HTNV infection, (2) how does HTNV block RIPK3-mediated cell death, and (3) what mechanism is STAT1 inactivated by RIPK3 (steric hindrance or simply retention in the ER by RIPK3). Determining the answers to these questions is critical to elucidate the innate immune response against HTNV propagation and is of vital importance for developing efficient strategies for disease therapy.

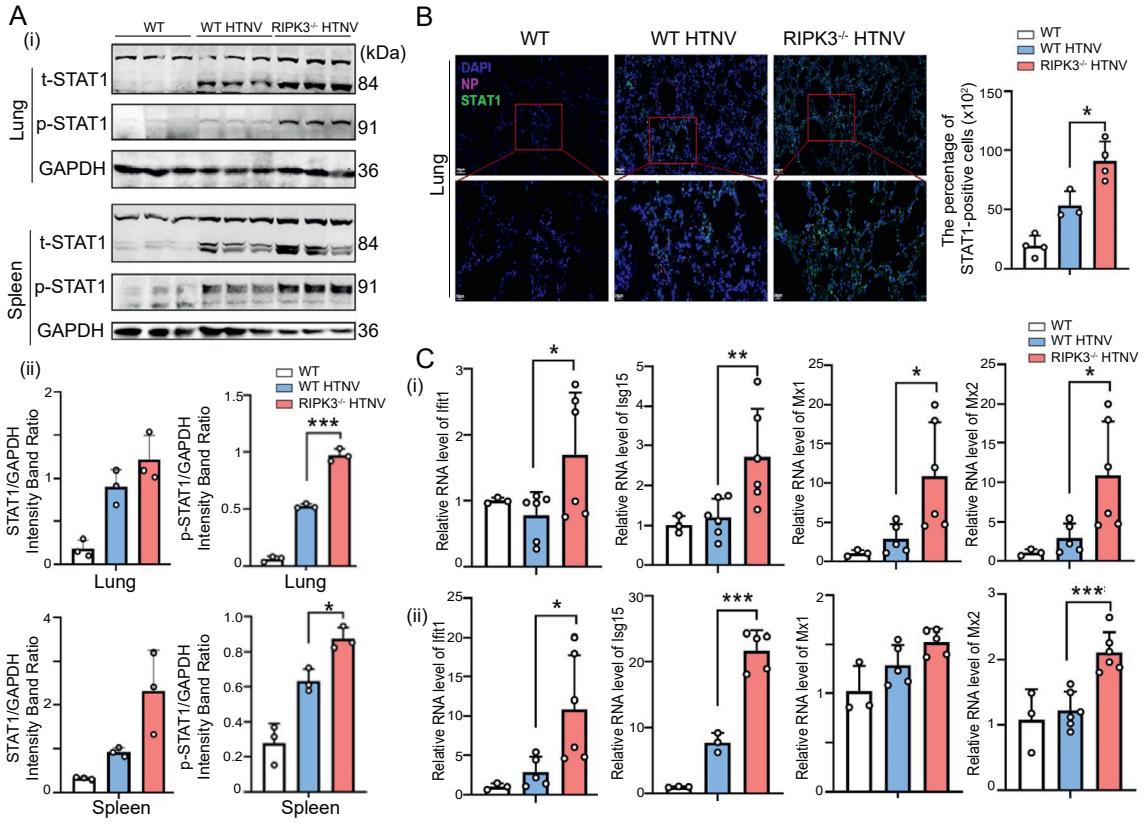

Fig. 6. RIPK3-deficient mice efficiently launched STAT1-mediated antiviral responses against HTNV infection. **A** Expression levels of JAK-STAT pathway indicators in lung and spleen samples obtained from WT and RIPK3$^{-/-}$ mice after viral challenge. Samples were collected at 9 dpi for immunoblotting (i). Densitometric analysis of the band intensity for p-STAT1 (ii). **B** Tissue immunofluorescence assay assays were conducted on lung samples from WT and RIPK3$^{-/-}$ mice after infection. HTNV NP (pink), STAT1 (green), and DAPI (blue). Immunofluorescence images are representative of at least three samples. We used ImageJ to measure the fluorescence intensity. After detecting the fluorescence area in the picture, we calculated the ratio of the green area (STAT1) to the blue area (DAPI), showing the percentage of STAT1-positive cells in the picture. Scale bars, 50 μm and 20 μm. **C** RNA collected from lung (i) and spleen (ii) samples from WT and RIPK3$^{-/-}$ mice after viral challenge. Samples were collected at 9 dpi to measure the level of ISGs using qRT-PCR. Data represent the mean ± SD. $^{*}P < 0.05$, $^{**}P < 0.01$, and $^{***}P < 0.001$.

Regarding HTNV infection activates RIPK3 activation, we speculate that TLR3 plays a crucial role in this process. RIG-like receptors (RLRs, e.g., RIG-I and MDA5) and Toll-like receptors (TLRs, e.g., TLR3 and TLR4) assist host cells in recognizing HTNV and promote strong antiviral immunity (Zhang et al., 2014). TLR-TRIF-TBK1 and RIG-I-MAVS-TBK1 are crucial pathways that activate IFN responses (Tartey and Takeuchi, 2017). Activated IRF3 recruits and phosphorylates IRF3/IRF7. IRF3 and IRF7 homodimers translocate to the nucleus and initiate IFN transcription. Notably, TLR3 was reported to initiate necroptosis indirectly by TNF activation or directly by the TRIF-RIPK3-MLKL axis (Kaiser et al., 2013), which indicates a crosstalk between the TLR3 pathway and RIPK3 signaling. This hypothesis requires further investigation.

Regarding activated-RIPK3 does not trigger necroptosis during HTNV infection, this might be because multiple biological processes are manipulated by HTNV. RIPK3-MLKL-mediated necroptosis exerts antiviral activity in BMDMs against multiple viruses by destroying viral reservoirs (Bedient et al., 2020; Gaba et al., 2019; Pasparakis and Vandenabeele, 2015; Zheng et al., 2020). Crimean-Congo hemorrhagic fever virus (CCHFV) is a member of the Nairovirus genus and the *Bunyaviridae* family (Schnittler and Feldmann, 2003). The NP of CCHFV triggered apoptosis by activating caspase-3 during the late stages of infection in SW-13 cells (Karlberg et al., 2011). However, no evidence suggests that hantavirus infection directly caused apparent cell death or morphological alterations either *in vivo* or *in vitro*. Here, we showed that HTNV-infected BMDMs did not undergo a notable change in cell death, which is also in line with the current hypothesis that monocytes and macrophages act as viral reservoirs to facilitate hantaviral propagation (Scholz et al., 2017). TSZ-stimulated cell death depends on the binding of TNF-α to the TNF receptor (TNFR) in the absence of cIAP1/2 combined with caspase inhibition. Then, the downstream signal triggers formation of the necrosome complex, which is composed of RIPK1 and RIPK3 (Hussain et al., 2018). We also found that TSZ-stimulated cell death was not prevented by HTNV infection in L929 cells. MLKL, an executor molecule for necroptosis, has necroptosis-independent functions, such as its roles in receptor internalization, ligand–receptor degradation, endosomal trafficking, extracellular vesicle formation, autophagy, and inflammasome regulation (Martens et al., 2021). We reported that HTNV could dynamically regulate host autophagy to interrupt PRR signaling (Wang et al., 2019), indicating that MLKL could be exploited by HTNV to enhance autophagy rather than cell death. Further exploration into the mechanism by which HTNV infection antagonizes cell death is needed.

Regarding the specific mechanism that STAT1 is inactivated by RIPK3, our data suggest several possibilities. RIPK3 could interact with STAT1 (Fig. 3A–E), as a point mutant of RIPK3 without kinase activity also blocked HTNV-induced STAT1 activation (Fig. 3I). Based on this, RIPK3 might cause steric hindrance by blocking the phosphorylation sites of STAT1. Notably, RIPK3 also sequestered STAT1 near the nucleus (Fig. 3A), and the retention of STAT1 by RIPK3 might restrict STAT1 activation. Finally, RIPK3 ablation could also promote the expression of total STAT1 (Fig. 2E–G), which suggested that RIPK3 might regulate not only the phosphorylation but also the transcription of STAT1. Further experiments are required to elucidate the specific mechanisms.

Determining the ideal cell and animal models for HTNV infection was the focus of experiments. Studies have shown that monocytes and

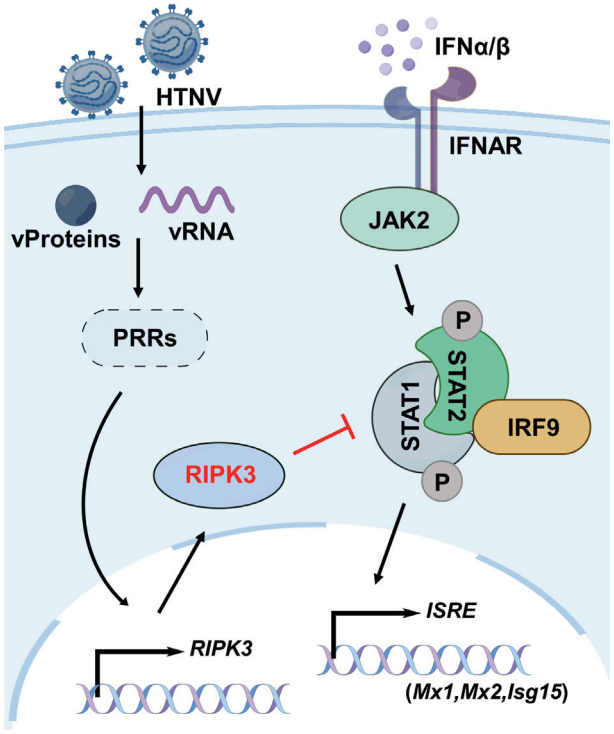

Fig. 7. Schematic illustration showing the mechanism behind HTNV's ability to evade IFN responses during late infection. After HTNV infection, RIPK3 expression was upregulated, resulting in downregulated ISG expression. In this process, RIPK3 interacts with STAT1 through its nonkinase domain. This interaction suppresses the phosphorylation and activation of STAT1, which limits the secretion of ISGs, including *Mx1* and *Isg15*. RIPK3 could play a non-canonical role in regulating HTNV replication and the inflammatory response through the JAK-STAT pathway.

macrophages (Mo/Mφ) are ideal cell types to investigate the mechanisms of hantaviral replication *in vitro* (Ermonval et al., 2016). We previously found that HTNV infection could modulate Mo/Mφ polarization, which then triggered type I IFN responses to suppress viral infection (Yang et al., 2022). Recent research indicated that HTNV (high lethality) replicated more effectively than PUUV (low lethality) in Mo/Mφ, while nonpathogenic hantaviruses did not produce any detectable progeny viruses, suggesting that the replication capacity of hantaviruses in Mo/Mφ may be positively correlated with their virulence (Raftery et al., 2020). Hence, Mo/Mφ, including primary BMDMs and the RAW264.7 cell line, can be used as target cells to explore antiviral mechanism against HTNV infection. Additionally, no disease model that faithfully recapitulates HFRS (HTNV infection causes asymptomatic infection in rodents) is available (Gowen and Hickerson, 2017). Previous studies have confirmed that HTNV could lead to lethal infection in suckling mice, probably resulting from a neurological defect that is uncharacteristic of human HFRS (Golden et al., 2015). Here, we investigated the role of RIPK3 in host innate immunity during HTNV infection based on a macrophage cell model and C57BL/6J mouse model, both of which are accepted hantaviral models.

ISGs are cellular factors induced by the IFN-mediated innate immune response to resist and control pathogens. ISG products have diverse roles and include antiviral effectors and negative and positive regulators of IFN signaling (Schneider et al., 2014). Additionally, RIPK3 has been reported to regulate type I IFN production in IAV-infected BMDMs via interaction with RIG-I/MAVS and activation of protein kinase R (PKR), a critical regulator of IFN-β mRNA stability (Downey et al., 2017). We found that RIPK3 regulated the expression of MX1, MX2, IFIT1 and ISG15. Mx, induced by type I IFN, is among the ISGs produced by host cells and has a wide range of antiviral effects and GTPase activity. *In vitro* and *in vivo* experiments have shown that Mx genes can be transcribed and translated only in the presence of type I IFN, double-stranded RNA or viral infection to aid pathogen invasion resistance. Mx was found to induce hydrolysis of the viral nucleocapsid through its GTPase activity to restrict virus replication (Fuchs et al., 2017; Haller et al., 2007). IFIT1 is a member of the IFIT family that can recognize several types of RNAs, including 5′-triphosphate RNA and 5′ capped 2′-O unmethylated mRNA (Daffis et al., 2010). Previous studies found that IFIT1 could inhibit JEV replication by binding 5′-capped 2′-O unmethylated RNA (Kimura et al., 2013), and positively regulating IFN production to regulate Alphavirus genome translation (Reynaud et al., 2015). We measured the expression levels of IFIT1 using qRT–PCR, which were higher than those in the infected WT group. However, research has shown that IFIT1 cannot inhibit negative-sense RNA virus replication or pathogenesis either *in vitro* or *in vivo*, including those of the *Orthomyxoviridae*, *Bunyaviridae*, and *Filoviridae* families (Pinto et al., 2015). Its role in restricting hantavirus infection remains unclear. ISG15 exerts an antiviral effect by covalently binding viral and cellular target proteins, inhibiting virion release or regulating virus latency. Furthermore, the ISG15 monomer can promote natural killer (NK) cell proliferation and dendritic cell (DC) maturation and enhance the chemotactic activity of neutrophils (Perng and Lenschow, 2018). ISG15 has been found to inhibit the replication of a variety of viruses, such as influenza virus (IV), Newcastle disease virus (DNV), JEV, VSV, Ebolavirus-like particles (VLPs) and dengue virus (DENV) (Dai et al., 2011; Giannakopoulos et al., 2009; Hsiang et al., 2009; Hsiao et al., 2010; Malakhova and Zhang, 2008; Orinska et al., 2005; Wu et al., 2020). In addition to the ISGs mentioned above, OAS1, IFIT2 and IFIT3 were upregulated through IRF3 translocation, which activated an IFN response after HTNV infection (Ye et al., 2015). Among the limitations of this study are that the molecular detection of antiviral ISGs was incomplete. We found that multiple ISGs were upregulated in RIPK3 knockout BMDMs, and these ISGs might synergistically defend against HTNV infection.

5. Conclusion

In conclusion, our study confirmed that RIPK3 could interact with STAT1 and regulate its phosphorylation at Ser727, thus promoting HTNV replication by inhibiting the expression of ISGs. Given that JAK/STAT/ISG signaling plays an essential role in anti-HTNV immunity, RIPK3 may have potential therapeutic implications for the prevention and treatment of human diseases caused by HTNV.

Data availability

All the data generated during this study are included in the manuscript.

Ethics statement

This article does not contain any studies with human subjects performed by any of the authors. The mouse experiments were conducted in compliance with a protocol approved by the Institutional Animal Care and Use Committee of Air Force Medical University. (Animal Experimental Welfare & Ethical Inspection number: 20230015).

Author contributions

Yue Si: conceptualization, formal analysis, investigation, writing-original draft, writing-review and editing. Haijun Zhang, Ziqing Zhou and Xudong Zhu: data curation, methodology, writing-original draft. Yongheng Yang, He Liu, Liang Zhang, Linfeng Cheng and Kerong Wang: methodology, visualization. Wei Ye, Xin Lv: formal Analysis. Hongwei

Ma: project administration. Xijing Zhang, Wugang Hou, Gang Zhao, Yingfeng Lei and Fanglin Zhang: conceptualization, funding acquisition, resources, supervision, writing-review and editing.

Conflict of interest

The authors declare no competing interests.

Acknowledgements

This work was supported in whole or in part by the National Natural Science Foundation of China (82172272, 31970148 and 82222367), and the Key Research and Development Program of Shaanxi (2021ZDLSF01-05 and 2021ZDLSF01-02).

Appendix A. Supplementary data

Supplementary data to this article can be found online at https://doi.org/10.1016/j.virs.2023.08.006.

References

Bedient, L., Pokharel, S.M., Chiok, K.R., Mohanty, I., Beach, S.S., Miura, T.A., Bose, S., 2020. Lytic cell death mechanisms in human respiratory syncytial virus-infected macrophages: roles of pyroptosis and necroptosis. Viruses 12, 932.

Bian, P., Ye, C., Zheng, X., Luo, C., Yang, J., Li, M., Wang, Y., Yang, J., Zhou, Y., Zhang, F., Lian, J., Zhang, Y., Jia, Z., Lei, Y., 2020. RIPK3 promotes JEV replication in neurons via downregulation of IFI44L. Front. Microbiol. 11, 368.

Christgen, S., Tweedell, R.E., Kanneganti, T.D., 2022. Programming inflammatory cell death for therapy. Pharmacol. Ther. 232, 108010.

Daffis, S., Szretter, K.J., Schriewer, J., Li, J., Youn, S., Errett, J., Lin, T.Y., Schneller, S., Zust, R., Dong, H., Thiel, V., Sen, G.C., Fensterl, V., Klimstra, W.B., Pierson, T.C., Buller, R.M., Gale Jr., M., Shi, P.Y., Diamond, M.S., 2010. 2′-O methylation of the viral mRNA cap evades host restriction by IFIT family members. Nature 468, 452–456.

Dai, J., Pan, W., Wang, P., 2011. ISG15 facilitates cellular antiviral response to dengue and west nile virus infection in vitro. Virol. J. 8, 468.

Dermentzaki, G., Politi, K.A., Lu, L., Mishra, V., Pérez-Torres, E.J., Sosunov, A.A., McKhann 2nd, G.M., Lotti, F., Shneider, N.A., Przedborski, S., 2019. Deletion of Ripk3 prevents motor neuron death in vitro but not in vivo. eNeuro 6, ENEURO.0308-18.2018.

Downey, J., Pernet, E., Coulombe, F., Allard, B., Meunier, I., Jaworska, J., Qureshi, S., Vinh, D.C., Martin, J.G., Joubert, P., Divangahi, M., 2017. RIPK3 interacts with MAVS to regulate type I IFN-mediated immunity to Influenza A virus infection. PLoS Pathog. 13, e1006326.

Ermonval, M., Baychelier, F., Tordo, N., 2016. What do we know about how hantaviruses interact with their different hosts? Viruses 8, 223.

Fuchs, J., Hölzer, M., Schilling, M., Patzina, C., Schoen, A., Hoenen, T., Zimmer, G., Marz, M., Weber, F., Müller, M.A., Kochs, G., 2017. Evolution and antiviral specificities of interferon-induced Mx proteins of bats against ebola, influenza, and other RNA viruses. J. Virol. 91, e00361-17.

Gaba, A., Xu, F., Lu, Y., Park, H.S., Liu, G., Zhou, Y., 2019. The NS1 protein of influenza A virus participates in necroptosis by interacting with MLKL and increasing its oligomerization and membrane translocation. J. Virol. 93, e01835-18.

Giannakopoulos, N.V., Arutyunova, E., Lai, C., Lenschow, D.J., Haas, A.L., Virgin, H.W., 2009. ISG15 Arg151 and the ISG15-conjugating enzyme UbE1L are important for innate immune control of Sindbis virus. J. Virol. 83, 1602–1610.

Golden, J.W., Hammerbeck, C.D., Mucker, E.M., Brocato, R.L., 2015. Animal models for the study of rodent-borne hemorrhagic fever viruses: arenaviruses and hantaviruses. BioMed Res. Int. 2015, 793257.

Gordon, S., Martinez, F.O., 2010. Alternative activation of macrophages: mechanism and functions. Immunity 32, 593–604.

Gowen, B.B., Hickerson, B.T., 2017. Hemorrhagic fever of bunyavirus etiology: disease models and progress towards new therapies. J. Microbiol. 55, 183–195.

Haller, O., Kochs, G., Weber, F., 2007. Interferon, Mx, and viral countermeasures. Cytokine Growth Factor Rev. 18, 425–433.

Handke, W., Oelschlegel, R., Franke, R., Krüger, D.H., Rang, A., 2009. Hantaan virus triggers TLR3-dependent innate immune responses. J. Immunol. 182, 2849–2858.

Hansen, L.W., Jacob, A., Yang, W.L., Bolognese, A.C., Prince, J., Nicastro, J.M., Coppa, G.F., Wang, P., 2018. Deficiency of receptor-interacting protein kinase 3 (RIPK3) attenuates inflammation and organ injury in neonatal sepsis. J. Pediatr. Surg. 53, 1699–1705.

Hardestam, J., Klingström, J., Mattsson, K., Lundkvist, A., 2005. HFRS causing hantaviruses do not induce apoptosis in confluent Vero E6 and A-549 cells. J. Med. Virol. 76, 234–240.

Heap, R.E., Marín-Rubio, J.L., Peltier, J., Heunis, T., Dannoura, A., Moore, A., Trost, M., 2021. Proteomics characterisation of the L929 cell supernatant and its role in BMDM differentiation. Life Sci. Alliance 4, e202000957.

Hsiang, T.Y., Zhao, C., Krug, R.M., 2009. Interferon-induced ISG15 conjugation inhibits influenza A virus gene expression and replication in human cells. J. Virol. 83, 5971–5977.

Hsiao, N.W., Chen, J.W., Yang, T.C., Orloff, G.M., Wu, Y.Y., Lai, C.H., Lan, Y.C., Lin, C.W., 2010. ISG15 over-expression inhibits replication of the Japanese encephalitis virus in human medulloblastoma cells. Antivir. Res. 85, 504–511.

Hussain, M., Zimmermann, V., van Wijk, S.J.L., Fulda, S., 2018. Mouse lung fibroblasts are highly susceptible to necroptosis in a reactive oxygen species-dependent manner. Biochem. Pharmacol. 153, 242–247.

Jiang, H., Du, H., Wang, L.M., Wang, P.Z., Bai, X.F., 2016. Hemorrhagic fever with renal syndrome: pathogenesis and clinical picture. Front. Cell. Infect. Microbiol. 6, 1.

Kaiser, W.J., Sridharan, H., Huang, C., Mandal, P., Upton, J.W., Gough, P.J., Sehon, C.A., Marquis, R.W., Bertin, J., Mocarski, E.S., 2013. Toll-like receptor 3-mediated necrosis via TRIF, RIP3, and MLKL. J. Biol. Chem. 288, 31268–31279.

Kariwa, H., Yoshimatsu, K., Arikawa, J., 2007. Hantavirus infection in East Asia. Comp. Immunol. Microbiol. Infect. Dis. 30, 341–356.

Karlberg, H., Tan, Y.J., Mirazimi, A., 2011. Induction of caspase activation and cleavage of the viral nucleocapsid protein in different cell types during Crimean-Congo hemorrhagic fever virus infection. J. Biol. Chem. 286, 3227–3234.

Kimura, T., Katoh, H., Kayama, H., Saiga, H., Okuyama, M., Okamoto, T., Umemoto, E., Matsuura, Y., Yamamoto, M., Takeda, K., 2013. Ifit1 inhibits Japanese encephalitis virus replication through binding to 5′ capped 2′-O unmethylated RNA. J. Virol. 87, 9997–10003.

Koehler, H., Cotsmire, S., Zhang, T., Balachandran, S., Upton, J.W., Langland, J., Kalman, D., Jacobs, B.L., Mocarski, E.S., 2021. Vaccinia virus E3 prevents sensing of Z-RNA to block ZBP1-dependent necroptosis. Cell Host Microbe 29, 1266–1276.e1265.

Laskowski, R.A., 2001. PDBsum: summaries and analyses of PDB structures. Nucleic Acids Res. 29, 221–222.

Lee, A.J., Ashkar, A.A., 2018. The dual nature of type I and type II interferons. Front. Immunol. 9, 2061.

Li, B., Wang, X., Yu, M., Yang, P., Wang, W., 2020. G6PD, bond by miR-24, regulates mitochondrial dysfunction and oxidative stress in phenylephrine-induced hypertrophic cardiomyocytes. Life Sci. 260, 118378.

Lu, D.H., Jiang, H., Lian, J.Q., 2021. Hantavirus infection during pregnancy. Virol. Sin. 36, 345–353.

Ma, H., Han, P., Ye, W., Chen, H., Zheng, X., Cheng, L., Zhang, L., Yu, L., Wu, X., Xu, Z., Lei, Y., Zhang, F., 2017a. The long noncoding RNA NEAT1 exerts antihantaviral effects by acting as positive feedback for RIG-I signaling. J. Virol. 91, e02250-16.

Ma, H.W., Ye, W., Chen, H.S., Nie, T.J., Cheng, L.F., Zhang, L., Han, P.J., Wu, X.A., Xu, Z.K., Lei, Y.F., Zhang, F.L., 2017b. In-cell western assays to evaluate Hantaan virus replication as a novel approach to screen antiviral molecules and detect neutralizing antibody titers. Front. Cell. Infect. Microbiol. 7, 269.

Ma, R., Zhang, X., Shu, J., Liu, Z., Sun, W., Hou, S., Lv, Y., Ying, Q., Wang, F., Jin, X., Liu, R., Wu, X., 2021. Nlrc3 knockout mice showed renal pathological changes after HTNV infection. Front. Immunol. 12, 692509.

Malakhova, O.A., Zhang, D.E., 2008. ISG15 inhibits Nedd4 ubiquitin E3 activity and enhances the innate antiviral response. J. Biol. Chem. 283, 8783–8787.

Martens, S., Bridelance, J., Roelandt, R., Vandenabeele, P., Takahashi, N., 2021. MLKL in cancer: more than a necroptosis regulator. Cell Death Differ. 28, 1757–1772.

Meng, Y., Sandow, J.J., Czabotar, P.E., Murphy, J.M., 2021. The regulation of necroptosis by post-translational modifications. Cell Death Differ. 28, 861–883.

Mesev, E.V., LeDesma, R.A., Ploss, A., 2019. Decoding type I and III interferon signalling during viral infection. Nat. Microbiol. 4, 914–924.

Newton, K., Dugger, D.L., Wickliffe, K.E., Kapoor, N., de Almagro, M.C., Vucic, D., Komuves, L., Ferrando, R.E., French, D.M., Webster, J., Roose-Girma, M., Warming, S., Dixit, V.M., 2014. Activity of protein kinase RIPK3 determines whether cells die by necroptosis or apoptosis. Science 343, 1357–1360.

Nguyen, L.N., Kanneganti, T.D., 2022. PANoptosis in viral infection: the missing puzzle piece in the cell death field. J. Mol. Biol. 434, 167249.

Ning, T., Wang, L., Liu, S., Ma, J., Nie, J., Huang, W., Li, X., Li, Y., Wang, Y., 2021. Monitoring neutralization property change of evolving Hantaan and Seoul viruses with a novel pseudovirus-based assay. Virol. Sin. 36, 104–112.

Orinska, Z., Bulanova, E., Budagian, V., Metz, M., Maurer, M., Bulfone-Paus, S., 2005. TLR3-induced activation of mast cells modulates CD8+ T-cell recruitment. Blood 106, 978–987.

Park, K., Kim, W.K., Lee, S.H., Kim, J., Lee, J., Cho, S., Lee, G.Y., No, J.S., Lee, K.H., Song, J.W., 2021. A novel genotype of Hantaan orthohantavirus harbored by *Apodemus agrarius* chejuensis as a potential etiologic agent of hemorrhagic fever with renal syndrome in Republic of Korea. PLoS Negl. Trop. Dis. 15, e0009400.

Pasparakis, M., Vandenabeele, P., 2015. Necroptosis and its role in inflammation. Nature 517, 311–320.

Perng, Y.C., Lenschow, D.J., 2018. ISG15 in antiviral immunity and beyond. Nat. Rev. Microbiol. 16, 423–439.

Pinto, A.K., Williams, G.D., Szretter, K.J., White, J.P., Proença-Módena, J.L., Liu, G., Olejnik, J., Brien, J.D., Ebihara, H., Mühlberger, E., Amarasinghe, G., Diamond, M.S., Boon, A.C., 2015. Human and murine IFIT1 proteins do not restrict infection of negative-sense RNA viruses of the Orthomyxoviridae, Bunyaviridae, and Filoviridae families. J. Virol. 89, 9465–9476.

Raftery, M.J., Abdelaziz, M.O., Hofmann, J., Schönrich, G., 2018. Hantavirus-driven PD-L1/PD-L2 upregulation: an imperfect viral immune evasion mechanism. Front. Immunol. 9, 2560.

Raftery, M.J., Lalwani, P., Lütteke, N., Kobak, L., Giese, T., Ulrich, R.G., Radosa, L., Krüger, D.H., Schönrich, G., 2020. Replication in the mononuclear phagocyte system (MPS) as a determinant of hantavirus pathogenicity. Front. Cell. Infect. Microbiol. 10, 281.

Reynaud, J.M., Kim, D.Y., Atasheva, S., Rasalouskaya, A., White, J.P., Diamond, M.S., Weaver, S.C., Frolova, E.I., Frolov, I., 2015. IFIT1 differentially interferes with translation and replication of alphavirus genomes and promotes induction of type I interferon. PLoS Pathog. 11, e1004863.

Saleh, D., Najjar, M., Zelic, M., Shah, S., Nogusa, S., Polykratis, A., Paczosa, M.K., Gough, P.J., Bertin, J., Whalen, M., Fitzgerald, K.A., Slavov, N., Pasparakis, M., Balachandran, S., Kelliher, M., Mecsas, J., Degterev, A., 2017. Kinase activities of RIPK1 and RIPK3 can direct IFN-β Synthesis induced by lipopolysaccharide. J. Immunol. 198, 4435–4447.

Salentin, S., Schreiber, S., Haupt, V.J., Adasme, M.F., Schroeder, M., 2015. PLIP: fully automated protein-ligand interaction profiler. Nucleic Acids Res. 43, W443–W447.

Schneider, W.M., Chevillotte, M.D., Rice, C.M., 2014. Interferon-stimulated genes: a complex web of host defenses. Annu. Rev. Immunol. 32, 513–545.

Schnittler, H.J., Feldmann, H., 2003. Viral hemorrhagic fever – a vascular disease? Thromb. Haemost. 89, 967–972.

Scholz, S., Baharom, F., Rankin, G., Maleki, K.T., Gupta, S., Vangeti, S., Pourazar, J., Discacciati, A., Höijer, J., Bottai, M., Björkström, N.K., Rasmuson, J., Evander, M., Blomberg, A., Ljunggren, H.G., Klingström, J., Ahlm, C., Smed-Sörensen, A., 2017. Human hantavirus infection elicits pronounced redistribution of mononuclear phagocytes in peripheral blood and airways. PLoS Pathog. 13, e1006462.

Shrum, B., Anantha, R.V., Xu, S.X., Donnelly, M., Haeryfar, S.M., McCormick, J.K., Mele, T., 2014. A robust scoring system to evaluate sepsis severity in an animal model. BMC Res. Notes 7, 233.

Solà-Riera, C., García, M., Ljunggren, H.G., Klingström, J., 2020. Hantavirus inhibits apoptosis by preventing mitochondrial membrane potential loss through up-regulation of the pro-survival factor BCL-2. PLoS Pathog. 16, e1008297.

Steere, A.C., Green, J., Hutchinson, G.J., Rahn, D.W., Pachner, A.R., Schoen, R.T., Sigal, L.H., Taylor, E., Malawista, S.E., 1987. Treatment of Lyme disease. Zentralblatt Bakteriol Mikrobiol Hyg. Ser. A Med. Microbiol. Infect. Dis. Virol. Parasitol. 263, 352–356.

Sulzbacher, M.M., Sulzbacher, L.M., Passos, F.R., Bilibio, B.L.E., de Oliveira, K., Althaus, W.F., Frizzo, M.N., Ludwig, M.S., Da Cruz, I.B.M., Heck, T.G., 2022. Adapted murine sepsis score: improving the research in experimental sepsis mouse model. BioMed Res. Int. 2022, 5700853.

Tariq, M., Kim, D.M., 2022. Hemorrhagic fever with renal syndrome: literature review, epidemiology, clinical picture and pathogenesis. Infect. Chemother. 54, 1–19.

Tartey, S., Takeuchi, O., 2017. Pathogen recognition and Toll-like receptor targeted therapeutics in innate immune cells. Int. Rev. Immunol. 36, 57–73.

Villarino, A.V., Kanno, Y., O'Shea, J.J., 2017. Mechanisms and consequences of Jak-STAT signaling in the immune system. Nat. Immunol. 18, 374–384.

Wang, K., Ma, H., Liu, H., Ye, W., Li, Z., Cheng, L., Zhang, L., Lei, Y., Shen, L., Zhang, F., 2019. The glycoprotein and nucleocapsid protein of hantaviruses manipulate autophagy flux to restrain host innate immune responses. Cell Rep. 27, 2075–2091.e2075.

Wang, P.Z., Li, Z.D., Yu, H.T., Zhang, Y., Wang, W., Jiang, W., Bai, X.F., 2012. Elevated serum concentrations of inflammatory cytokines and chemokines in patients with haemorrhagic fever with renal syndrome. J. Int. Med. Res. 40, 648–656.

Weigert, M., Binks, A., Dowson, S., Leung, E.Y.L., Athineos, D., Yu, X., Mullin, M., Walton, J.B., Orange, C., Ennis, D., Blyth, K., Tait, S.W.G., McNeish, I.A., 2017. RIPK3 promotes adenovirus type 5 activity. Cell Death Dis. 8, 3206.

Wu, J., Zhu, K., Luo, X., Han, Y., Zhang, B., Wang, Z., Dong, S., Zou, X., Chen, X., Liu, H., Wu, T., Zheng, Z., Xie, Y., Zhao, J., Liu, Y., Wen, Z., Liu, D., Wang, Y., Zheng, S., Huang, X., Jing, C., Yang, G., 2020. PM(2.5) promotes replication of VSV by ubiquitination degradation of phospho-IRF3 in A549 cells. Toxicol. In Vitro 62, 104698.

Xu, Z., Wei, L., Wang, L., Wang, H., Jiang, S., 2002. The in vitro and in vivo protective activity of monoclonal antibodies directed against Hantaan virus: potential application for immunotherapy and passive immunization. Biochem. Biophys. Res. Commun. 298, 552–558.

Yan, Y., Zhang, D., Zhou, P., Li, B., Huang, S.Y., 2017. HDOCK: a web server for protein-protein and protein-DNA/RNA docking based on a hybrid strategy. Nucleic Acids Res. 45, W365–W373.

Yang, Y., Li, M., Ma, Y., Ye, W., Si, Y., Zheng, X., Liu, H., Cheng, L., Zhang, L., Zhang, H., Zhang, X., Lei, Y., Shen, L., Zhang, F., Ma, H., 2022. LncRNA NEAT1 potentiates SREBP2 activity to promote inflammatory macrophage activation and limit Hantaan virus propagation. Front. Microbiol. 13, 849020.

Ye, W., Xu, Y., Wang, Y., Dong, Y., Xi, Q., Cao, M., Yu, L., Zhang, L., Cheng, L., Wu, X., Xu, Z., Lei, Y., Zhang, F., 2015. Hantaan virus can infect human keratinocytes and activate an interferon response through the nuclear translocation of IRF-3. Infect. Genet. Evol. J. Mol. Epidemiol. Evol. Genet. Infect. Dis. 29, 146–155.

Yiang, G.T., Chen, Y.H., Chou, P.L., Chang, W.J., Wei, C.W., Yu, Y.L., 2013. The NS3 protease and helicase domains of Japanese encephalitis virus trigger cell death via caspase-dependent and -independent pathways. Mol. Med. Rep. 7, 826–830.

Yin, H., Wang, Z., Yang, S., Zheng, X., Bao, Y., Lin, W., Huang, C., Qiu, L., 2022. Taurine inhibits necroptosis helps to alleviate inflammatory and injury induced by Klebsiella infection. Vet. Immunol. Immunopathol. 250, 110444.

Zhan, Q., Jeon, J., Li, Y., Huang, Y., Xiong, J., Wang, Q., Xu, T.L., Li, Y., Ji, F.H., Du, G., Zhu, M.X., 2022. CAMK2/CaMKII activates MLKL in short-term starvation to facilitate autophagic flux. Autophagy 18, 726–744.

Zhang, Y., Liu, B., Ma, Y., Yi, J., Zhang, C., Zhang, Y., Xu, Z., Wang, J., Yang, K., Yang, A., Zhuang, R., Jin, B., 2014. Hantaan virus infection induces CXCL10 expression through TLR3, RIG-I, and MDA-5 pathways correlated with the disease severity. Mediat. Inflamm. 2014, 697837.

Zhang, Y., Ma, R., Wang, Y., Sun, W., Yang, Z., Han, M., Han, T., Wu, X.A., Liu, R., 2021. Viruses run: the evasion mechanisms of the antiviral innate immunity by Hantavirus. Front. Microbiol. 12, 759198.

Zhao, Q., Yu, X., Zhang, H., Liu, Y., Zhang, X., Wu, X., Xie, Q., Li, M., Ying, H., Zhang, H., 2017. RIPK3 mediates necroptosis during embryonic development and postnatal inflammation in FADD-deficient mice. Cell Rep. 19, 798–808.

Zheng, M., Williams, E.P., Malireddi, R.K.S., Karki, R., Banoth, B., Burton, A., Webby, R., Channappanavar, R., Jonsson, C.B., Kanneganti, T.D., 2020. Impaired NLRP3 inflammasome activation/pyroptosis leads to robust inflammatory cell death via caspase-8/RIPK3 during coronavirus infection. J. Biol. Chem. 295, 14040–14052.